International Journal of Wavelets, Multiresolution
and Information Processing
Vol. 4, No. 2 (2006) 239–251

World Scientific
www.worldscientific.com

EXTRACTION OF PARTICLE CONCENTRATION DISTRIBUTION FROM PLUG FLOW CT IMAGES USING 3D WAVELET MULTIRESOLUTION

M. TAKEI* and M. OCHI

Department of Mechanical Engineering, Nihon University,
1-8-14 Kanda Surugadai Tokyo 101-8308, Japan
**takei@mech.cst.nihon-u.ac.jp*

Y. SAITO

Hosei University, 3-7-2 Kajino Tokyo 184-0002, Japan

K. HORII

Shirayuri College, 1-25 Midorigaoka, Tokyo 182-8525, Japan

Particle concentration distribution images of a dense solid-air two-phase (plug) flow have been obtained at 10 ms intervals at a bend pipe upstream in a horizontal pipeline by means of a capacitance computed tomography. The three-dimensional images (time and two-dimensional space images) have been decomposed to the wavelet time levels to extract the dominant particle concentration distribution using three-dimensional discrete wavelet multiresolution. As a result, the time dominant particle distribution with specific time frequency level is visualized in a cross-section. In detail, the high concentration of the particle spatial distribution at the dense flow front, which composes high-time frequency levels 6 and 7, is located at the center above the stationary layer.

Keywords: Capacitance CT; 3D wavelets; solid-air two-phase flow; image processing.

AMS Subject Classification: 65T60, 76T25, 68U10

1. Introduction

A dense solid-air two-phase (plug) flow in a pipeline is typically used in various industries, such as the chemical, pharmaceutical and food industries. Conventionally, studies are conducted from a macroscopic viewpoint, such as the relationship among solid flow rate, gas flow rate, pressure drop and plug length[1,2] and pressure drop prediction.[3] On the other hand, studies have been conducted from a microscopic viewpoint in order to achieve higher performance in pneumatic conveyance because the detailed energy loss between particles is able to be considered. For example, Klinzing[4] pointed out particle movement consisting of a plug qualitatively. Tsuji carried out a computer simulation of particle movement by

the Discrete Elements Method (DEM).[5] Moreover, quantitatively, the velocity of particles composing a plug front end was measured at cross-sectional grids in a pipeline by means of the Laser Doppler Velocimeter (LDV), to clarify the particle movement patterns.[6] Also, an optical fiber probe system was produced to measure particle distribution.[7] However, since the LDV method cannot measure the entire cross-section, it is difficult to understand three-dimensional (two spatial dimensions and one time dimension) particle movement in a dense flow. Also, the optical fiber probe is intrusive. Under these circumstances, non-invasive capacitance CT has been studied as a technique by which to visualize particle behavior in a cross-section of a pipeline.[8] In capacitance CT, a sensor comprising many electrodes is arranged around the circumference of a pipeline, in order to measure the capacitances between the electrodes. On the basis of permittivity distribution in the cross-section, particle concentration distribution is obtained via reconstruction. This system is applied to fluidized bed coalescence,[9] bubble formation[10] and pneumatic conveyance.[11]

However, the images obtained by capacitance CT are blurred, because approximate values are resolved using a mathematically ill-posed inverse problem. Image analysis is necessary in order to extract the features of the blurred images, so as to ascertain the dominant particles from the image. Currently, in engineering fields, discrete wavelet analysis is being performed using image analysis rather than Fourier transform.[12] The merit of discrete wavelet analysis is its ability to analyze frequency, while not removing time and space information. The orthonormal transform of this analysis enables quantitative decomposition and re-composition of a picture image. A number of researchers have applied this idea to the analysis of the flow images such as shear stress image[13] and stream line.[14] Two-dimensional wavelet transform has been used to obtain the two-dimensional original image. This means that fewer studies of three-dimensional wavelet analysis[15] are applied to the 3D flow image. Especially, it is very useful to analyze the particle concentration patterns in the dense flow by means of the decomposition of 3D dense flow CT images from the viewpoint of detail energy loss and multiphase flow dynamics.

The originality of the present method lies in the application of the three-dimensional discrete wavelet multiresolution analysis to a three-dimensional capacitance CT image, in order to extract the particle pattern features in particle dense flow upstream of a pipe bend. In the present study, particle capacitances upstream of a pipe bend were measured to reconstruct the particle concentration images in two-dimensional space and time. The images were multi-resolved by three-dimensional discrete wavelets, in order to extract the dominant time particle levels.

2. Experiments

2.1. *Capacitance computed tomography*

The capacitance CT sensor is shown in Fig. 1. Insulation materials separate the 12 electrodes in the sensor.[16] The relationship between capacitance and permittivity

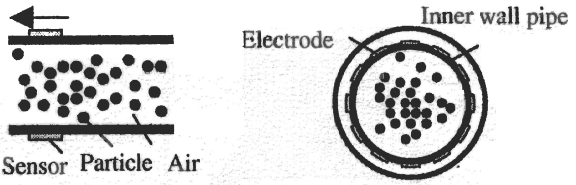

(A) Frontal view (B) Cross-sectional view

Fig. 1. Overview of capacitance computed tomography.

in the electrostatic field is expressed by:

$$C_{i,j} = -\frac{\varepsilon_0}{V_c} \oint_{r \subseteq \Gamma_j} \varepsilon(\boldsymbol{r}) \nabla V_i(\boldsymbol{r}) \cdot d\boldsymbol{r}, \tag{2.1}$$

where i is the standard electrode number, which ranges from 1 to 11; j is the reference electrode number, which ranges from $i+1$ to 12; $C_{i,j}$ is the measured capacitance between standard electrode i and reference electrode j; ε_0 is the vacuum permittivity; $\varepsilon(\boldsymbol{r})$ is the relative permittivity distribution on the cross-section; $\boldsymbol{r}$ is a position vector on the cross-section: $\boldsymbol{r} = (x, y)$; V_c is the known voltage to the ith electrode, Γ_j is the area affected by the electric line of force, and $V_i(\boldsymbol{r})$ is the potential distribution on the cross-section between the ith and jth electrodes. Even though $\varepsilon(\boldsymbol{r})$ and $V_i(\boldsymbol{r})$ are unknown, $\varepsilon(\boldsymbol{r})$ in Eq. (2.1) can be approximately solved when total capacitance is assumed to be the linear coupling of electric charge at position $\boldsymbol{r}$ with weight of sensitivity in the Γ_j area. When a particle exists only at $\boldsymbol{r} = \boldsymbol{r}_0$ between i and j electrodes, and air exists at other positions, the Laplace equation

$$\nabla \cdot [\varepsilon(\boldsymbol{r}) \nabla V(\boldsymbol{r})] = 0 \tag{2.2}$$

is assumed in the cross-section. Equation (2.2) is discretized using the Finite Element Method (FEM) and $V_i(\mathbf{r})$ distribution is obtained with the boundary condition for substitution into Eq. (2.1). Capacitance value $C_{i,j}$ with a particle at $\boldsymbol{r} = \boldsymbol{r}_0$ is then obtained. In this condition, a sensitivity value with a particle at $\boldsymbol{r} = \boldsymbol{r}_0$ is calculated from:

$$S_{i,j}^{\mathbf{r0}} = \left(\frac{1}{\beta}\right) \frac{C_{i,j}^{\mathbf{r0}} - C_{i,j}^{\text{air}}}{C_{i,j}^{\text{particle}} - C_{i,j}^{\text{air}}}, \quad \beta = \left(\frac{D^2}{N_x N_y}\right) \Big/ \pi \left(\frac{D}{2}\right)^2, \tag{2.3}$$

where $C_{i,j}^{\text{air}}$ and $C_{i,j}^{\text{particle}}$ are the capacitances when particles and air occupy the pipe cross-section, respectively. The coefficient β represents an area ratio of one pixel to the whole pipe cross-section, and D is diameter of pipe and N_x and N_y are x and y axial space resolutions as shown in Fig. 2. The sensitivity values are repeatedly

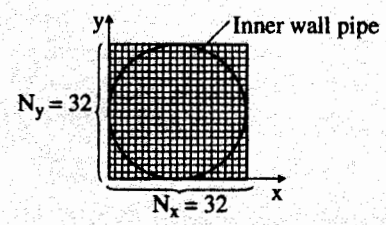

Fig. 2. Space resolution.

obtained from Eqs. (2.2) and (2.3) at every position and every pair of electrodes. Finally, $C_{i,j}$ is expressed by linear coupling of $\varepsilon(\boldsymbol{r})$ with weight of $S^{\mathrm{T}}_{i,j}$, that is:

$$C_{i,j} = \sum_{r=(1,1)}^{(Nx,Ny)} S^{\mathrm{T}}_{i,j}\varepsilon(\boldsymbol{r}). \tag{2.4}$$

Moreover, Eq. (2.4) was rewritten using matrix expression as:

$$\mathbf{C} = \mathbf{S_e E}. \tag{2.5}$$

In other words, capacitance CT can be used to obtain the permittivity distribution of particles $\mathbf{E}$ in the cross-section from both known sensitivity map matrix $\mathbf{S_e}$ and measured capacitance matrix $\mathbf{C}$. In the case of 12 electrodes and $32 \times 32 = 1024$ pixels, as in the spatial resolution shown in Fig. 2, in the pipe cross-section the sensitivity map $\mathbf{S_e}$ is a 66×1024 pixel matrix in Eq. (2.5). Capacitance matrix $\mathbf{C}$ expresses a 66×1 column vector, and permittivity distribution matrix $\mathbf{E}$ is a 1024×1 column vector. The mathematical method used to obtain permittivity matrix $\mathbf{E}$ from both capacitance matrix $\mathbf{C}$ and sensitivity map matrix $\mathbf{S_e}$ is an ill-posed inverse problem, because inverse matrix $\mathbf{S_e}^{-1}$ does not exist.

2.2. *Experimental equipment, conditions and method*

Equipment for the present experiment comprised a feeder tank, a pipeline of 49.0 mm inside diameter, a receiver tank and a Root's blower, as shown in Fig. 3. A CT sensor with 12 electrodes was arranged around the pipe circumference upstream of the pipe bend. Air intake volume was $0.019\,\mathrm{m^3/s}$, and particle was supplied at 390.0 g/s. The mean air velocity in the pipeline, as calculated from the air volume, was 9.10 m/s. The Reynolds number was 2.92×10^4; the solid air ratio was 12.46. The particles were polyethylene pellets that were almost spherical, having a diameter of 3.26 mm and a concentration of $910\,\mathrm{kg/m^3}$. Polyethylene pellets were charged with more static electricity than the air, because the specific permittivity of polyethylene pellets (2.3) is higher than that of air (1.0). In Eq. (2.5), the image re-constitution process for obtaining unknown $\mathbf{E}$ from measured value $\mathbf{C}$ and already known $\mathbf{S_e}$ is an ill-posed inverse problem; namely, the unknown number is larger than the expression number. Theoretically, the solution is present infinitely.

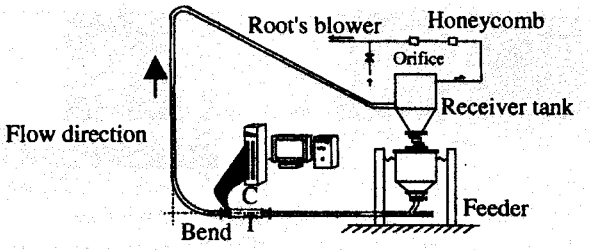

Fig. 3. Experimental equipment.

In this study, the dielectric constants, which show particle concentration distribution, were determined by the Newton Raphson Method. In the present study, permittivity matrix **E**, which indicates particle two-dimensional space distribution at a particular time, is normalized via calibration using a maximum value of 1.0 and a minimum value of 0.0. The maximum value indicates the situation wherein the particles occupy the entire cross-section, the minimum value the situation wherein the air occupies the entire cross-section. One image pixel is 1.53×1.53 mm^2. The inside cross-section (49.0 mm) is divided by 32×32 image pixels. When a particle core passes through the measurement section, the diameter of one particle takes up 2.13 image pixels, because the particle diameter is 3.26 mm. The time interval necessary to acquire one frame is $\Delta t = 10.0$ ms. For analysis in the next section, 512 consecutive frames for 5,120.0 ms are selected from among the total reconstructed frames obtained for 60.0 seconds.

2.3. *Experimental results*

Representative particle concentration images $\mathbf{E_{xyt}}$ from $50\,\Delta t$ to $200\,\Delta t$ at $50\,\Delta t$ step ($\Delta t = 10$ ms) are shown in Fig. 4. The image pixel, at which no particle exists, is blue. As particle concentration on an image pixel becomes high, the image pixel turns red, as shown in the color bar. Upstream of a pipe bend, particles in the dense flow are accumulated, resulting in plug flow. A plug flow is a special case of dense flow, which the whole cross-section is occupied by the particles. From Fig. 4, on the whole, the time-transient distributions of particle concentration are qualitatively visualized. To roughly confirm particle movement during the time, the spatial mean particle concentration at a time is calculated by

$$\overline{D_p}(t) = \frac{1}{(N_x N_y - N_{\text{out}})} \sum_{y=1}^{N_y} \sum_{x=1}^{N_x} \mathbf{E_{xyt}}, \tag{2.6}$$

where, N_{out} is the pixel number outside the pipe (see Fig. 5). This figure reveals that five dense flows passed through the pipe cross-section during the time (denoted by 1, 2, 3, 4 and 5). Three dense flows (1, 2 and 3) plugged the pipe cross-section entirely; however, two dense flows (4 and 5) did not plug the pipe cross-section. In

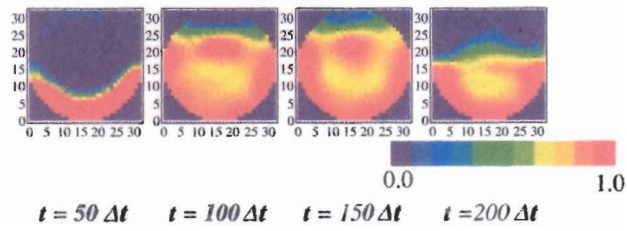

Fig. 4. Representative Images of particle concentration.

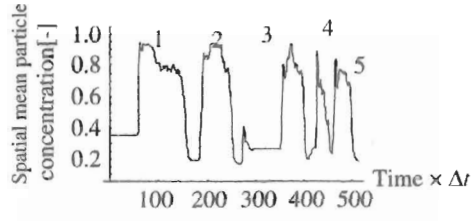

Fig. 5. Spatial mean particle concentration.

the next section, the highly dense flows (1, 2 and 3) were analyzed by the three-dimensional wavelet multiresolution.

3. Image Analysis and Discussion

3.1. *3D discrete wavelet multiresolution*

In this section, the 3D wavelet transform is explained by the matrix form. $\mathbf{E_{xyt}}$, a three-dimensional original image comprising $N_x \times N_y \times N_t$ pixels to the three-dimensional wavelet spectrum $\mathbf{S_{tyx}}$, is obtained by

$$\mathbf{S_{tyx}} = [\mathbf{W_t}[\mathbf{W_y}[\mathbf{W_x}\mathbf{E_{xyt}}]^{\mathbf{T}}]^{\mathbf{T}}]^{\mathbf{T}}, \tag{3.1}$$

where N_x, N_y and N_t are pixels in the x, y (space axis) and t (time axis) dimensions, respectively, and $\mathbf{W_x}$, $\mathbf{W_y}$ and $\mathbf{W_t}$ are the analyzing wavelet matrices comprising $N_x \times N_x$ pixels, $N_y \times N_y$ pixels and $N_t \times N_t$ pixels, respectively. The transpose matrices are:

$$[\mathbf{E_{xyt}}]^{\mathbf{T}} = \mathbf{E_{txy}}, \quad [\mathbf{E_{txy}}]^{\mathbf{T}} = \mathbf{E_{ytx}}, \quad [\mathbf{E_{ytx}}]^{\mathbf{T}} = \mathbf{E_{xyt}}. \tag{3.2}$$

Therefore, the wavelet spectrum $\mathbf{S_{tyx}}$ comprises $N_t \times N_y \times N_x$ pixels. The inverse three-dimensional wavelet transform of Eq. (3.1) is expressed as

$$\mathbf{E_{xyt}} = [\mathbf{W_x}[\mathbf{W_y}[\mathbf{W_t}\mathbf{S_{tyx}}]^{\mathbf{T}}]^{\mathbf{T}}]^{\mathbf{T}}. \tag{3.3}$$

For second-order Daubechies orthonormal functions of the analyzing wavelets and the original image data comprising $N_x = N_y = 32$, $N_t = 512$, the original image can be decomposed to the time frequency levels; namely,

$$\begin{aligned} \mathbf{E_{xyt}} &= \mathbf{E_0} + \mathbf{E_1} + \mathbf{E_2} + \mathbf{E_3} + \mathbf{E_4} + \mathbf{E_5} + \mathbf{E_6} + \mathbf{E_7} + \mathbf{E_8} + \mathbf{E_9}, \\ \mathbf{E_0} &= [\mathbf{W_x}[\mathbf{W_y}[\mathbf{W_t}\mathbf{S_0}]^{\mathbf{T}}]^{\mathbf{T}}]^{\mathbf{T}}, \quad \mathbf{E_1} = [\mathbf{W_x}[\mathbf{W_y}[\mathbf{W_t}\mathbf{S_1}]^{\mathbf{T}}]^{\mathbf{T}}]^{\mathbf{T}}, \\ &\cdots \\ \mathbf{E_8} &= [\mathbf{W_x}[\mathbf{W_y}[\mathbf{W_t}\mathbf{S_8}]^{\mathbf{T}}]^{\mathbf{T}}]^{\mathbf{T}}, \quad \mathbf{E_9} = [\mathbf{W_x}[\mathbf{W_y}[\mathbf{W_t}\mathbf{S_9}]^{\mathbf{T}}]^{\mathbf{T}}]^{\mathbf{T}}, \end{aligned} \tag{3.4}$$

where $\mathbf{S_0}$ is the lowest frequency spectrum and $\mathbf{S_9}$ the highest. Therefore, the image inversely transformed from $\mathbf{S_0} : \mathbf{E_0}$, indicates the particle two-dimensional space distribution having the lowest time frequency, which is referred to as time level 0. Time level 0 thus indicates the least unsteady and temporary space distribution. On the other hand, the image inversely transformed from $\mathbf{S_9} : \mathbf{E_9}$, indicates the two-dimensional space distribution having the highest time frequency, which is referred to as time level 9. The time level 9 therefore indicates the most time-fluctuated space distribution. If the pixel order of the initial 3D original image is $N_t \times N_x \times N_y$ pixels in Eq. (3.1), the decomposed image in Eq. (3.4) indicates the x space- and t time-directional particle distribution having the various y directional space frequencies. Figure 6 is the above-mentioned resolution process. All elements added from time levels 0 to 9 recover the original three-dimensional image because of the orthonormal transform of discrete wavelets. From this three-dimensional wavelet multiresolution, the dominant particle concentration distribution is realized. Figure 7 shows the matrix element values, $\mathbf{W_x}$ and $\mathbf{W_y}$, of the analyzing wavelets matrix of the Daubechies function of second order in the case of 32 pixels. The matrix element value in the case of 512 pixels, $\mathbf{W_t}$, is obtained by magnifying Fig. 7, which is not shown in this figure. The relationship between wavelet levels

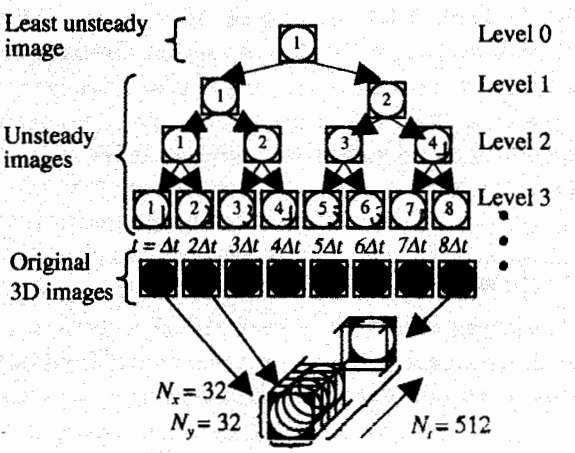

Fig. 6. Multiresolution by 3D wavelets.

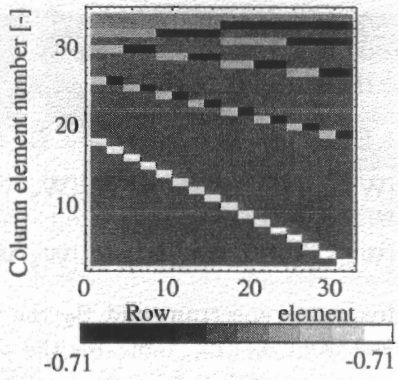

Fig. 7. Analyzing wavelet matrix.

Table 1. Relationship between wavelet level and representative frequency.

Time level	Time frequency [Hz]	Time mean frequency [Hz]
0	0.150–0.195	0.17
1	0.195–0.390	0.29
2	0.390–0.586	0.49
3	0.586–0.781	0.68
4	0.781–1.953	1.37
5	1.953–3.320	2.64
6	3.320–7.227	5.27
7	7.227–14.84	11.03
8	14.84–30.85	22.85
9	30.85–50.00	40.3

and representative space frequencies obtained from the absolute values by Fourier transform is shown in Table 1 for the case of $\Delta t = 10\,\text{ms}$. The time frequency is shown only in this figure because the decomposition direction is the only time in this study. In the different pixel order, the other space frequency is able to be calculated based on the same idea. The representative time frequency is the frequency indicating the highest value in the wavelet level band. Each level operates a kind of band-pass filter.

3.2. *Wavelet multiresolution to time*

The three-dimensional original images of particle concentration in Fig. 4 are decomposed by the three-dimensional wavelet multiresolution of Eq. (3.4). The lowest time frequency of time level 0 indicates the least unsteady two-dimensional space distribution of particle concentration during that time. The highest time frequency of time level 9 indicates the most unsteady distribution of particle concentration. Figure 8 shows an example of decomposed images from the original image at $100\,\Delta t$,

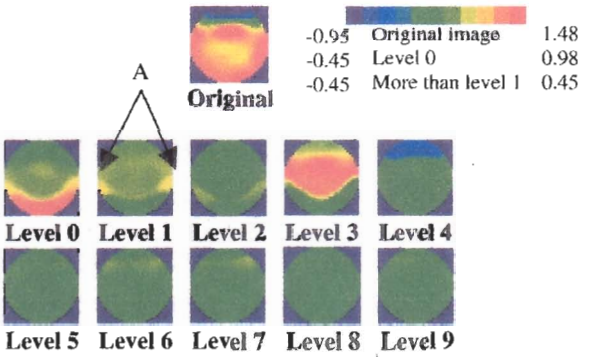

Fig. 8. Original and decomposed images at $100\,\Delta t$.

which is the middle part of dense flow 1, according to Fig. 5. The color map values differ among the original, the level 0 and the higher than level 1 images. The summation of all level images at each space element completely recovers the original image in Fig. 4, due to the orthonormal wavelet transform. From Fig. 8, the lowest frequency level 0 indicates the time-mean particle concentration spatial distribution; namely, the distribution is mainly a stationary layer, which is located at the pipeline bottom. Also, Fig. 8 reveals that the relative low frequency level 3 dominates particle movement at $100\,\Delta t$ among these levels, the spatial particle distribution in level 3 being located above the stationary layer of the time-mean location in level 0. Moreover, in levels 1 and 2, both sides above the stationary layer have slightly yellow portions (denoted by A), indicating that the particle concentration is changed at these portions with low frequency.

To confirm dominant levels of total particle movement, the spatial-mean values of particle concentration images decomposed by wavelets multiresolution are calculated by

$$\overline{D_p^L}(t,L) = \frac{1}{(N_y N_x - N_{\text{out}})} \sum_{\text{y=1}}^{\text{Ny}} \sum_{\text{x=1}}^{\text{Nx}} \mathbf{E}_{\mathbf{xy}}^{\mathbf{L}}, \tag{3.5}$$

where $\mathbf{E}_{\mathbf{xy}}^{\mathbf{L}}$ is the level L image decomposed by multiresolution at time t. Figure 9 is the result from level 0 to level 7. Levels 8 and 9 are omitted because they do not show clear peaks. The vertical axis is the spatial mean particle concentration, calculated from the deviation image for subtraction of the time-space mean concentration value from the original concentration image pixels. In level 3, three high values denoting 1, 2 and 3 are visible at the periods from $65\,\Delta t$ to $128\,\Delta t$, from $193\,\Delta t$ to $250\,\Delta t$, and from $354\,\Delta t$ to $384\,\Delta t$, which are equivalent to the numbers in Fig. 5. The particle concentration of each level at the start and end times of those periods are visualized for detailed discussion of particle movement. First, period 1 is discussed. Just before the start time, at $64\,\Delta t$, in levels 6 and 7, a high value appears (denoted by 1-s) that indicates the front of the start time. At the end time of period 1, $132\,\Delta t$,

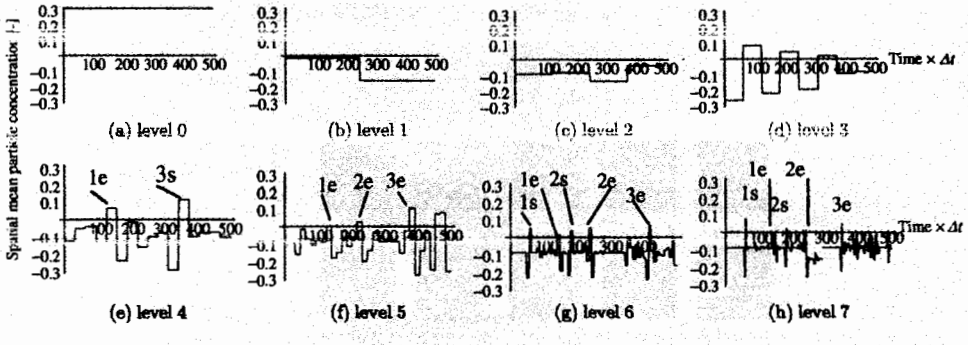

Fig. 9. Spatial mean value of decomposed images.

in levels 4 and 5, a high value appears (denoted by 1-e). As time goes on, at 148 Δt in levels 6 and 7, a high value appears and moves to 156 Δt in level 7, (denoted by 1-e). Next, period 2 is discussed. At 192 Δt, in levels 6 and 7, a high value appears (denoted by 2-s). At the end time of period 2, 240 Δt, the high value is slightly apparent (denoted by 2-e) in level 5. As time goes on, at 243 Δt, in level 6 (denoted by 2-e) a high value appears and moves to 250 Δt in level 7 (denoted by 2-e).

The figure reveals that at the start time of each period, a high value appears in a high level and moves to higher levels as the time passes.

3.3. *Multiresolution images and discussion*

Next, we focused on the start and end times of the first period to confirm the flow pattern in detail. Figure 10 shows the decomposed images of the front and rear of the dense flow at periods 1, 2 and 3. The horizontal axis is the time and the vertical axis is the wavelet levels. The color bar is the same as in Fig. 8. At 64 Δt in Fig. 10(A), indicating the front of the dense flow, the values in high levels of levels 6 and 7 are high; however, the values in high levels of levels 3, 4 and 5 are nearly zero. This means that high-time frequency particles comprise the front of the dense flow. Moreover, the particle spatial distribution is located at the upper part of the stationary layer in the high frequency. To be precise, in level 6, the high value is located at the upper part (denoted by B) just over the stationary layer (denoted by C). In level 7, the high value is also located at the stationary layer (denoted by D). From 65 Δt to 128 Δt when the main body passes, the low level 3 is dominant. At 132 Δt indicating the rear of the dense flow, the high particle concentration is shown in levels 4 and 5; however, the particle concentration is low in levels 5 and 6. As time goes on to 148 Δt, the high concentration is seen in levels 6 and 7; however, particle concentration is low in level 5. Moreover, at 156 Δt, high concentration is seen only in level 7; the high concentration then disappears at 157 Δt.

With regards to the spatial distribution, at 132 Δt, a high-concentration portion is located at the top in level 5; the high-concentration portion then moves to the

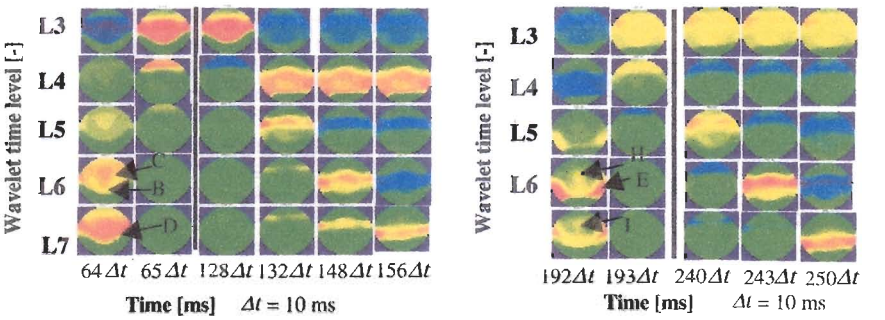

(A) Period 1 : Time 64-156 Δt. (B) Period 2 : Time 192-250 Δt.

Fig. 10. Front and rear of dense flow.

middle in level 6 at 148 Δt, and to the bottom in level 7 at 156 Δt. In other words, as time passes, the dominant level moves from level 5 to level 7, and the dominant spatial portions move from the top to the bottom. From the discussion, it is clear that the front of the dense flow is steep, part passing through the cross-section at high-time period indicating levels 6 and 7; on the other hand, the rear slopes gently, indicating gradual change from level 4 to level 7. Moreover, the decomposed levels of 6 and 7 images at 64 Δt in Fig. 10 reveal that the particles composing the dense flow at the front are discharged toward the front air phase. From these figures, it is predicted that particles at a front portion of the plug are discharged into the air phase in front of the plug near the center.

Period 2 in Fig. 10(B) has a tendency similar to period 1. Specifically, at plug front portion 192Δt of period 2, high particle concentration exists in the stationary layer upper part on both sides at time levels 6 and 7 (See arrow E). Relatively high particle concentration exists above the center of the cross-section. (See arrows H and I.) The time level 3 is dominant from 193 Δt to 240 Δt, while the plug main portion passes at period 2. The high-concentration particle is located at the stationary layer upper part. At 240 Δt, which is the plug end of period 2, comparatively high particle concentration is found in the pipeline section at the upper part of time level 5. At 243 Δt, the high particle concentration moves to the cross-sectional central portion at time level 6. At 250 Δt, the high particle concentration moves to pipeline bottom at time level 7.

This clear decomposition of the detailed particle movement in the plug flow is contributed by 3D wavelet multiresolution from the 3D particle density CT images. In detail, the capacitance CT technique visualizes the time transitional particle images in the cross-section. However, it is not easy to understand the temporary particle movement from the direct CT images because the images do not include the time frequency information. The 3D wavelet multiresolution overcomes the difficulties because it has characteristics to decompose the 2D special images with various time frequencies. However, it is impossible for the previous combination of LDV and Fourier analysis to achieve that.

4. Conclusions

The dominant time levels of dense flow in a pipeline cross-section were determined using capacitance computed tomography (CT) and three-dimensional wavelet multiresolution to analyze the particle concentration of the dense flow at a bend upstream. The following findings were obtained:

(1) According to this novel method, the particle concentration distribution of pipeline cross-sections of a dense solid air two-phase flow is extracted as dominant time levels. This clear extraction contributes to understanding in detail the 2D special particle distribution with dominant time frequency.
(2) The formation of particle concentration at the front of a dense flow comprises levels 6 and 7, indicating the high-time frequency level. The high concentration of particle spatial distribution is located more in the upper portion than just over the stationary layer, ensuring that the particles comprising the dense flow at the front are steeper than at the rear. The particles comprising the dense flow at the front are discharged toward the front air phase; moreover, it is possible to visualize discharging particle distribution in detail.
(3) Particle concentration at the rear of the dense flow moves from level 5 to level 7; moreover, the dominant spatial portion moves from top to bottom as time passes. It indicates the dense flow formation, whose rear slopes gently.

References

1. D. Mason, P. Marjanovic and A. Levy, A simulation system for pneumatic conveying systems, *Powder Technol.* **95** (1998) 7–14.
2. D. Chen, J. F. Flausner and R. Mei, A fluid mechanics approach to describing the behavior of pneumatically conveyed powder plugs, *Powder Technol.* **124** (2002) 127–137.
3. B. Mi and P. W. Wypych, Pressure drop prediction in low-velocity pneumatic conveying, *Powder Technol.* **81** (1994) 125–137.
4. G. E. Klinzing, Dense phase (Plug) conveying — observations and projections, *Handbook of Conveying and Handling of Particulate Solids*, ed. A. Levy and H. Kalman (Elsevier Science, 2001), pp. 329–341.
5. Y. Tsuji, T. Tanaka and T. Ishida, Langrangian numerical simulation of plug flow cohesionless particles in a horizontal pipe, *Powder Technol.* **71** (1992) 239–250.
6. M. Takei, M. Ochi, Y. Ishikawa and H. Nishimura, Movement of particles composing plug at front end, *Trans. Jpn. Soc. Mech. Eng.* **64**(628) (1998) 86–92 (in Japanese).
7. J. Hong and Y. Tomita, Measurement of distribution of solids concentration on high density gas-solids flow using an optical-fiber probe system, *Powder Technol.* **83** (1995) 85–91.
8. S. M. Huang, A. B. Plaskowski, C. G. Xie and M. S. Beck, Tomographic imaging of two-component flow using capacitance sensors, *J. Phys. E, Sci. Instrum.* **22** (1989) 173–177.
9. J. S. Halow and P. Nicoletti, Observations of fluidized bed coalescence using capacitance imaging, *Powder Technol.* **69** (1992) 255–277.

10. S. J. Wang, T. Dyakowski, C. G. Xie, R. A. Williams and M. S. Beck, Real time capacitance imaging of bubble formation at the distributor of a fluidized bed, *Chem. Eng. J.* **56**(3) (1995) 95–100.
11. T. Dyakowski, S. P. Luke, K. L. Ostrowski and R. A. Williams, On-line monitoring of dense phase flow using real time dielectric imaging, *Powder Technol.* **104** (1999) 287–295.
12. E. Hernandez and G. Weiss, First Course on Wavelets (CRC Press, 1996).
13. V. M. Poty and W. Lefer, A wavelet decomposition scheme and compression method for streamline-based vector field visualizations, *Comput. Graph.* **26**(6) (2002) 899–906.
14. M. Kimura, M. Takei, C. M. Ho, Y. Saito and K. Horii, Visualization of shear stress with micro imaging chip and discrete wavelets transform, *J. Fluid Eng. Trans. ASME* **124**(4) (2002) 1018–1024.
15. L. Pastor, A. Rodríguez, J. Espadero and L. Rincón, 3D wavelet-based multiresolution object representation, *Pattern Recogn.* **34**(12) (2001) 2497–2513.
16. W. Q. Yang, Hardware design of electrical capacitance tomography systems, *Meas. Sci. Technol.* **7**(3) (1996) 225–232.